




Low-temperature acanthite-like phase of Cu₂S: Electronic and transport propertiesHo Ngoc Nam ^{1,2,*}, Katsuhiro Suzuki,² Tien Quang Nguyen ², Akira Masago,³ Hikari Shinya,^{3,4,5} Tetsuya Fukushima,^{3,6,7} and Kazunori Sato ^{2,3}¹*Department of Precision Science and Technology, Graduate School of Engineering, Osaka University, 2-1 Yamadaoka, Suita, Osaka 565-0871, Japan*²*Division of Materials and Manufacturing Science, Graduate School of Engineering, Osaka University, 2-1 Yamadaoka, Suita, Osaka 565-0871, Japan*³*Center for Spintronics Research Network, Graduate School of Engineering Science, Osaka University, Toyonaka, Osaka 560-8531, Japan*⁴*Research Institute of Electrical Communication, Tohoku University, Sendai, Miyagi 980-8577, Japan*⁵*Center for Spintronics Research Network, Tohoku University, Sendai, Miyagi 980-8577, Japan*⁶*Institute of Solid State Physics, The University of Tokyo, 5-1-5 Kashiwanoha, Kashiwa, Chiba, 277-8581, Japan*⁷*Institute for AI and Beyond, The University of Tokyo, Bunkyo-ku, Tokyo 113-8656, Japan*

(Received 18 October 2021; revised 22 December 2021; accepted 14 February 2022; published 22 February 2022)

The mobility and disorder in the lattice of Cu atoms as liquidlike behavior is an important characteristic affecting the thermoelectric properties of Cu₂S. In this study, using a theoretical model called an acanthite-like structure for Cu₂S at a low-temperature range, we systematically investigate the electronic structure, intrinsic defect formation, and transport properties by first-principles calculations. Therefore, previous experimental reports on the indirect band-gap nature of Cu₂S were confirmed in this work with an energy gap of about 0.9–0.95 eV. As a result, the optical absorption coefficient estimated from this model also gives a potential value of $\alpha > 10^4 \text{ cm}^{-1}$ in the visible spectrum range. According to the bonding analysis and formation energy aspect, Cu vacancy is the most preferred defect to form in Cu₂S, which primarily affects the conductive behavior as a *p* type, as experimentally observed. Finally, the transport properties of Cu₂S system were successfully reproduced using an electron-phonon scattering method, highlighting the important role of relaxation time prediction in conductivity estimation instead of regarding it as a constant.

DOI: [10.1103/PhysRevB.105.075205](https://doi.org/10.1103/PhysRevB.105.075205)**I. INTRODUCTION**

Since its inception, thermoelectric (TE) technology has been proving its robust potential for harvesting waste heat and converting it into electricity [1,2]. This green solution turned out to be extremely useful in current circumstances, especially when fossil fuel resources are running out and the challenges of climate change are constantly increasing [3]. Many TE material generations have been explored with impressive performances as a result of these practical impetuses [4,5]. One of the most popular TE material paradigms called the “*phonon-glass electron-crystal*” (PGEC), was proposed in 1995 [6,7]. Interestingly, most of the state-of-the-art TE materials so far are in the PGEC paradigm with crystalline solid form. In nature, the thermal conductivity of liquids is known to be worse than that of solids, and this concept is a hint we can exploit to renovate the PGEC paradigm. Since 2012, such a TE material paradigm has been around, called a “*phonon-liquid electron-crystal*”, which takes advantage of the liquidlike behavior of superionic conductors in several materials to minimize thermal conductivity [8,9]. In particular, transition metal-chalcogenide compounds such as the (Ag,Cu)₂(S,Se,Te) group are typical materials for this concept with many fascinating properties and high TE performance [10–13].

Copper sulfide, or Cu_{2-x}S is inherently not only a well-known semiconductor for applications in photovoltaic solar cells [14,15], but recently it has also been recognized as a promising candidate for TE applications [16]. Although Cu₂S has been studied since the late 1940s, the thorough understanding of the crystal structure and electronic properties still has some ambiguity and controversy [17–19]. Referring to the crystal structure issue first, Cu_{2-x}S exists in many crystallographically distinct phases depending on the Cu content, such as chalcocite (Cu₂S), djurleite (Cu_{1.94}S), digenite (Cu_{1.8}S), and anilite (Cu_{1.75}S). In which, stoichiometric compound Cu₂S has three temperature-dependent phases including the γ phase (low-chalcocite or *L*-chalc. for temperatures below 378 K), the β phase (high-chalcocite or *H*-chalc. in the range of 378–698 K), and the α phase (above 698 K) [20].

However, it seems not to be that simple. The sensitivity to the temperature of Cu atoms makes them really mobile and disorderly, which is considered as liquidlike behavior. As a result, locating atoms becomes difficult and confusing in the study of their properties. For instance, in previous studies [21,22], the authors investigated the electronic structure of Cu₂S based on several artificial models for the high-temperature phase. Despite taking into account the experimentally determined low-temperature phase *L*-chalc., the results in these models still do not reproduce the band-gap energy or reveal the indirect nature as found in the experimental report [23,24]. The problem is, the *L*-chalc. phase is found

*honam@mat.eng.osaka-u.ac.jp

to have a large pseudo-orthorhombic structure including 96 molecular units (288 atoms) where each Cu atom has a unique site. Obviously, such a large number of atoms along with the low symmetry of the structure causes density functional theory (DFT) based investigations to be more challenging. Previous theoretical works approximated this structure by splitting it into two identical monoclinic cells (144 atoms per cell) to facilitate calculations [21,25]. However, for the investigation of electronic and transport properties, this structure is pretty large. The disorder of the Cu atoms and the large supercell size of *L*-chalc. phase can lead to the folding of *k* points at the Brillouin-zone (BZ) edge on the Γ point. Consequently, it can make the band gap direct while the evidence from the optical data shows that the nature of the band gap should be indirect.

In a recent structural investigation [26,27], the author used 15 potential crystal structures for Cu_2S (including the *L*-chalc. phase) to predict the most favored structure based on cohesive energy. Accordingly, the acanthite-like phase, which was derived from a similar low-temperature phase of Ag_2S , had the lowest energy among all. Interestingly, this acanthite-like structure is pretty simple. The arrangement of Cu and S atoms forms layered chains with a zig-zag shape where Cu atoms occupy only two order positions, tetrahedral and octahedral sites. As compared to the *L*-chalc. phase, there is not much difference in crystal (both are monoclinic) and electronic structure (except for direct/indirect nature) [26], hence several recent studies have adopted this acanthite-like model for calculations [28,29]. Therefore, it would be interesting to have insight into the physical properties of the acanthite-like phase, which can be a good alternative model of the *L*-chalc. phase for TE design applications at low temperatures.

In this work, we systematically investigate the electronic properties, the intrinsic point defect formation, and transport properties of the acanthite-like phase of Cu_2S by using first-principles calculations. In Sec. II A, the electronic structure of Cu_2S is considered using an acanthite-like model. In Sec. II B, the formation of point defects and diffusion behavior are also discussed as part of electronic properties. Finally, in Sec. II C, the transport properties of the acanthite-like model based on the electron-phonon scattering mechanism and the rationality of this model for TE design purposes are the main parts we focused on in this study.

II. COMPUTATIONAL METHODS

A. Electronic properties

Our DFT calculations are mainly carried out using the VASP code [30]. The projector-augmented wave (PAW) approach [31] is used with generalized gradient approximation (GGA) in the form of Perdue-Burke-Ernzerhof (PBE) [32]. Here, the $3d^{10}$ and $4s^1$ electrons of Cu, $3s^2$ and $3p^4$ electrons of S are treated as valence states. The wave functions are expanded in a plane-wave basis set with cut-off energy of 400 eV. A width of 0.05 eV of Gaussian smearing has been used in this work. All calculations were converged until the residual atomic force became smaller than 10^{-2} eV/Å. Since the DFT method is well-known for underestimating band-gap energy, the rotationally invariant DFT + *U* method with an

effective Hubbard parameter *U* of 7 eV [28,33], was applied to the *d* orbitals of Cu to handle on-site Coulomb interaction. Besides, we also employed the hybrid functional proposed by Heyd, Scuseria, and Ernzerhof (HSE06) [34] in several cases related to band structure calculations to compare with the results from the DFT + *U* method. The BZ was sampled using the Monkhorst-Pack *k*-mesh of $11 \times 9 \times 9$ for PBE functional, while a $8 \times 4 \times 4$ mesh was used for HSE06 functional. For defect formation calculations, a $2 \times 2 \times 2$ supercell with a corresponding $3 \times 3 \times 3$ *k*-mesh is used. The migration pathways of Cu vacancy were discussed as well, based on possible minimum energy pathways (MEP) between the adjacent sites using the nudged elastic band algorithm [35].

In the framework of band structure calculations, the linear optical properties can be obtained from the frequency-dependent complex dielectric function [36]:

$$\varepsilon(\omega) = \varepsilon_1(\omega) + i\varepsilon_2(\omega), \quad (1)$$

where $\varepsilon_1(\omega)$ and $\varepsilon_2(\omega)$ are the real and imaginary parts of the dielectric function, respectively; ω is the photon frequency. Consequently, the absorption coefficient $\alpha(\omega)$ is derived from $\varepsilon_1(\omega)$ and $\varepsilon_2(\omega)$ as follows:

$$\alpha(\omega) = \frac{\sqrt{2}\omega}{c} \left(\sqrt{\varepsilon_1^2 + \varepsilon_2^2} - \varepsilon_1 \right)^{\frac{1}{2}}. \quad (2)$$

In addition, the electric transition dipole moment (TDM) based on dipole transition matrix elements $P_{a \rightarrow b}$ between two states is defined as [37]

$$P_{a \rightarrow b} = \langle \psi_b | \mathbf{r} | \psi_a \rangle = \frac{i\hbar}{(E_b - E_a)m} \langle \psi_b | \mathbf{p} | \psi_a \rangle, \quad (3)$$

where ψ_a and ψ_b are eigenstates corresponding to energy E_a and E_b , m is the electron mass. It should be noted that for a more accurate band structure description, the meticulous estimation may necessitate calculations such as the GW-BSE method [38]. Only the predictions of the GGA + *U* and HSE06 functionals are considered here.

B. Intrinsic point defects formation

The defect formation energy $E_{\text{form}}(D, q)$ at charge state q of defect D as a function of Fermi energy can be defined as follows [39]:

$$E_{\text{form}}(D, q) = E_{D,q}^{\text{tot}} - E_{\text{bulk}}^{\text{tot}} + \sum n(i)\mu_i + q(E_{\text{VBM}} + \Delta E_{\text{Fermi}}), \quad (4)$$

where $E_{D,q}^{\text{tot}}$ is the total energy of the defect system, $E_{\text{bulk}}^{\text{tot}}$ is the total energy of the bulk system, n is the number of impurity atoms ($n > 0$ for doped atoms and $n < 0$ for removed atoms), μ_i is chemical potential of element i . E_{VBM} is referenced energy related to the valence band maximum (VBM) while ΔE_{Fermi} is Fermi energy relative to VBM. We also used simply core potential correction as a correction term for Eq. (4). Then, the chemical potential can be defined by relation $\mu_i = \mu_i^0 + \Delta\mu_i$, where μ_i^0 is total energy per atom of elemental solid i (for S, S_8 molecule is used, namely, $\mu_{\text{S}}^0 = \frac{1}{8}\mu_{\text{S}_8}^0$) and $\Delta\mu_i$ is condition to control the crystal growth. To

avoid the formation of elemental solid phase (i.e., precipitating) or unintended compounds (here, CuS and CuS₂ are used for competing phases), the following inequalities should be satisfied:

$$\Delta\mu_i \leq 0, \quad (5)$$

$$\Delta\mu_{\text{Cu}} + \Delta\mu_{\text{S}} \leq \Delta\mu(\text{CuS}), \quad (6)$$

$$\Delta\mu_{\text{Cu}} + 2\Delta\mu_{\text{S}} \leq \Delta\mu(\text{CuS}_2). \quad (7)$$

Lastly, the constraint is employed as the thermal equilibrium condition:

$$2\Delta\mu_{\text{Cu}} + \Delta\mu_{\text{S}} = \Delta\mu(\text{Cu}_2\text{S}), \quad (8)$$

where $\Delta\mu(X)$ is formation enthalpy of compound X. These values are calculated with $\Delta\mu(\text{CuS}) = -0.41$ eV, $\Delta\mu(\text{CuS}_2) = -0.31$ eV, and $\Delta\mu(\text{Cu}_2\text{S}) = -0.44$ eV. Defect formation energies are computed within the allowed region of $\Delta\mu_i$.

C. Transport properties: Electron-phonon coupling

For transport properties, the effect of electron-phonon coupling is investigated using the Quantum Espresso code [40]. Here, we used a plane-wave basis set with kinetic energy cut-offs of 60 and 600 Ry for wave functions and charge density, respectively. Besides, the uniform $12 \times 12 \times 12$ Γ -centered k -point and $3 \times 3 \times 3$ q -point grids are used for calculations. Then, the general transport parameters of the system are calculated using BoltzTraP code [41] to solve the semiclassical

Boltzmann transport equation within the relaxation-time approximation. The expressions for electrical conductivity (σ), Seebeck coefficient (S), electronic thermal conductivity (κ^e) are the following [42]:

$$\sigma_{\alpha\beta}(\mu, T) = K_{\alpha\beta}^{(0)}, \quad (9)$$

$$S_{\alpha\beta}(\mu, T) = k_B \sum_i (K_{\alpha\beta}^{(0)^{-1}})_{i\alpha} K_{i\beta}^{(1)}, \quad (10)$$

$$\kappa_{\alpha\beta}^e(\mu, T) = k_B^2 T \left[K_{\alpha\beta}^{(2)} - \sum_{ij} K_{\alpha i}^{(1)} (K^{(0)^{-1}})_{ij} K_{j\beta}^{(1)} \right], \quad (11)$$

where α, β, i, j are Cartesian components, μ is the chemical potential, T is the absolute temperature, k_B is the Boltzmann constant. Here, $K_{\alpha\beta}^{(p)}$ is the p th order electronic transport coefficient, which is defined as

$$K_{\alpha\beta}^{(p)}(\mu, T) = \frac{g_s e^{2-p}}{(2\pi)^3 (k_B T)^{p+1}} \sum_n \int_{\text{BZ}} d\mathbf{k} v_{n\mathbf{k}\alpha} v_{n\mathbf{k}\beta} \times \tau_{n\mathbf{k}}(\mu, T) I^{(p)}(\epsilon_{n\mathbf{k}}, \mu, T) \quad (12)$$

with g_s being the spin degeneracy, \mathbf{k} is the electron wave vector, $v_{\alpha\beta}$ is the electron group velocity, $\epsilon_{n\mathbf{k}}$ is the electron energy, and $I^{(p)}(\epsilon, \mu, T)$ is the material-independent integrand factor:

$$I^{(p)}(\epsilon, \mu, T) = (\epsilon - \mu)^p f(\epsilon, \mu, T) [1 - f(\epsilon, \mu, T)]. \quad (13)$$

Here, $f(\epsilon, \mu, T)$ is the Fermi-Dirac distribution function. The important factor in Eq. (12), electron energy relaxation time $\tau_{n\mathbf{k}}(\mu, T)$ can be defined by considering the electron-phonon coupling effect as follows:

$$\tau_{(\mu, T)}^{-1} = \frac{\Omega}{(2\pi)^2 \hbar} \sum_{mv} \int_{\text{BZ}} d\mathbf{q} |g_{mv}(\mathbf{k}, \mathbf{q})|^2 \{ [n(\omega_{\mathbf{v}\mathbf{q}}, T) + f(\epsilon_{m\mathbf{k}+\mathbf{q}}, \mu, T)] \delta(\epsilon_{n\mathbf{k}} + \omega_{\mathbf{v}\mathbf{q}} - \epsilon_{m\mathbf{k}+\mathbf{q}}) + [n(\omega_{\mathbf{v}\mathbf{q}}, T) + 1 - f(\epsilon_{m\mathbf{k}+\mathbf{q}}, \mu, T)] \delta(\epsilon_{n\mathbf{k}} - \omega_{\mathbf{v}\mathbf{q}} - \epsilon_{m\mathbf{k}+\mathbf{q}}) \}, \quad (14)$$

where Ω is the primitive cell volume, m is the electron band index, v is the phonon mode index, \mathbf{q} is the phonon wave vector, $\omega_{\mathbf{v}}$ is the phonon energy, $n(\omega, T)$ is the Bose-Einstein distribution function, and δ is the Dirac delta function. Besides, the Eliashberg spectral function related to electron-phonon coupling matrix elements $g_{mv}(\mathbf{k}, \mathbf{q})$ can be defined as [43]

$$\alpha^2 F(\omega) = \frac{1}{N(\epsilon_F)} \sum_{mn} \sum_{\mathbf{q}\mathbf{v}} \delta(\omega - \omega_{\mathbf{q}\mathbf{v}}) \sum_{\mathbf{k}} |g_{\mathbf{k}+\mathbf{q}, \mathbf{k}}^{\mathbf{q}\mathbf{v}, mn}|^2 \delta(\epsilon_{\mathbf{k}+\mathbf{q}, m} - \epsilon_F) \delta(\epsilon_{\mathbf{k}, n} - \epsilon_F). \quad (15)$$

However, it is worthy to note that the calculations describing full electron-phonon interaction [44] as in Eq. (14) are complicated and time consuming. Hence, in this study, we employed the electron-phonon average approximation (EPA) [42], which replaces the energy-dependent averages for their momentum-dependent quantities to handle $\tau_{n\mathbf{k}}(\mu, T)$ value. In detail, replacing $|g_{mv}(\mathbf{k}, \mathbf{q})|^2 \mapsto g_v^2(\epsilon_{n\mathbf{k}}, \epsilon_{m\mathbf{k}+\mathbf{q}})$ as the average electron-phonon matrix elements over the directions of \mathbf{k} and $\mathbf{k} + \mathbf{q}$ wave vectors, $\omega_{\mathbf{v}\mathbf{q}} \mapsto \bar{\omega}_{\mathbf{v}}$ as the average phonon energies over the cells of electron energy grids, and ρ is electron density of states:

$$\tau^{-1}(\epsilon, \mu, T) = \frac{2\pi\Omega}{g_s \hbar} \sum_{\mathbf{v}} \{ g_v^2(\epsilon, \epsilon + \bar{\omega}_{\mathbf{v}}) [n(\bar{\omega}_{\mathbf{v}}, T) + f(\epsilon + \bar{\omega}_{\mathbf{v}}, \mu, T)] \rho(\epsilon + \bar{\omega}_{\mathbf{v}}) + g_v^2(\epsilon, \epsilon - \bar{\omega}_{\mathbf{v}}) [n(\bar{\omega}_{\mathbf{v}}, T) + 1 - f(\epsilon - \bar{\omega}_{\mathbf{v}}, \mu, T)] \rho(\epsilon + \bar{\omega}_{\mathbf{v}}) \}. \quad (16)$$

III. RESULTS AND DISCUSSION

A. Electronic properties

Firstly, let us briefly mention the crystal structure issue, which strongly affects electronic structure. The acanthite-like

structure of Cu₂S was generated by substituting all Ag atoms with Cu atoms in the low-temperature phase of Ag₂S, and then the derived structure was fully relaxed using DFT. The optimized lattice parameters are shown in Table I. At the same cell size, the cohesive energy of the acanthite-like phase

TABLE I. The calculated lattice constants, average bond lengths, and cohesive energy per formula unit of the Cu_2S acanthite-like phase. For comparison with the L -chalc. phase, a $3 \times 2 \times 2$ supercell of acanthite-like phase is used. The average Cu-Cu bond length value of the L -chalc. phase (asterisk symbol) is referred from previous works [26,27].

	a (Å)	b (Å)	c (Å)	$\bar{d}_{\text{Cu}_1\text{-Cu}_1}$ (Å)	$\bar{d}_{\text{Cu}_1\text{-S}}$ (Å)	$\bar{d}_{\text{Cu}_1\text{-S}}$ (Å)	$\alpha = \gamma$ (°)	β (°)	E_{coh} (eV/f.u)
Acanthite-like (unit cell)	4.011	7.261	7.932	2.687	2.308	2.183	90	119.567	-11.659
Acanthite-like (super cell $3 \times 2 \times 2$)	12.042	14.504	15.862	2.687	2.308	2.182	90	119.598	-11.658
Low-chalcocite (Exp. [19])	13.494	11.884	15.246	2.65–2.69*	–	–	90	116.350	-11.637

is 20 meV lower than that of L -chalc. phase. This matches the results of a previous study with a value of 16 meV [27], indicating the thermodynamic stability of acanthite-like phase compared to L -chalc. phase. We also calculated the heat of formation of the acanthite-like phase compared with several structures at the stoichiometric limit and three different compounds of the Cu-S system in Fig. 1. We found that $\text{Cu}_{1.75}\text{S}$ (or Cu_7S_4) has the most stable structure among the Cu-S compounds considered, which was confirmed in a previous study [45]. However, at the stoichiometric limit, the acanthite-like phase is the most stable structure with the lowest formation energy. Comparing the acanthite-like phase to L -chalc. phase, the differences between two structures are the a and b lattice constants, and the disorder of Cu atoms in the compounds. In Fig. 2(b), a simple ab-initio molecular dynamics (AIMD) simulation at room temperature is used to observe the behavior of atoms in an acanthite-like phase. It can be seen that S atoms form a nearly immobile sub-lattice, while Cu atoms are conductors that move around disorderly as liquid behavior. Compared with the experimentally obtained L -chalc. phase, it shows the same behavior of S atoms with the zig-zag arrangement [see Fig. 2(c)]. However, it can be realized that the displacement of Cu atoms in the L -chalc. phase is more complicated, necessitating a thorough analysis of Cu displacement. In the latest research [29], the author has focused on AIMD simulations to investigate the displacement of Cu atoms in both structures. Accordingly, the radial and cumulative distribution functions of Cu-Cu, Cu-S, and S-S pairs showed a similar tendency in both acanthite-like and

L -chalc. phases. In addition, they also calculated the mean square displacement of Cu atoms, revealing that both phases have comparable Cu diffusion inside crystal structures.

Besides, the phonon dispersion was taken into account to ensure the stability of the acanthite-like phase [see Fig. 2(g)]. No imaginary frequency appeared in the phonon band structure, revealing that this structure is dynamically stable. It is important to note that there is the appearance of soft modes in the low-frequency range due to the low crystal symmetry, which leads to the drop-down of some optical modes to acoustic modes. This decrease in phonon frequency is usually associated with a certain type of phase transition. Based on the investigations noted above, it makes sense to utilize the acanthite-like model as the stable phase of Cu_2S at the stoichiometric limit for low-temperature transport properties investigations.

Minimizing the number of atoms compared to the L -chalc. phase not only reduces the computational cost but also gives us an insight into the electronic structure, where the states are not overlapping and overly dense. We then started investigating the electronic structure of this model using a GGA functional. Figure 2(d) shows that the GGA functional fails completely to reproduce the Cu_2S energy gap, which is experimentally reported as an indirect band gap of 1.1 eV [24]. This is not surprising because the GGA functional is known to frequently underestimate the bandgap. Moreover, the strongly correlated nature of transition metal d -layer electrons can also be a reason. Hence, the GGA + U method was used to improve the bandgap estimation. It can be seen that the Hubbard potential U hardly changes the band edge compared to GGA, the conduction band (CB) is only pushed to the higher energy side than the valence band (VB). As a result, an indirect energy gap of 0.91 eV appears, which is in agreement with the result of previous theoretical work [28]. For further insight, we also examined the band structure using HSE06 functional, which is known to reproduce the bandgap energy of semiconductors better than GGA. The band edge given by HSE06 functional is pretty similar to the GGA + U description with VBM located at the Γ point. Meanwhile, the conduction band minimum (CBM) is distorted along the Γ -A direction, reproducing a slightly wider indirect band gap of 0.95 eV compared to the GGA + U result. The second CBM has a slight difference as GGA + U shows that it is located between the Y-C range while HSE06 shows it is located at the Y-point, which may lead to some difference in observing the optical transition states afterward. However, both functions have similar descriptions of the atomic orbital contributions and their density of states (DOS). The predominance of Cu d orbitals with S p orbitals forms the VB. At the same time, the

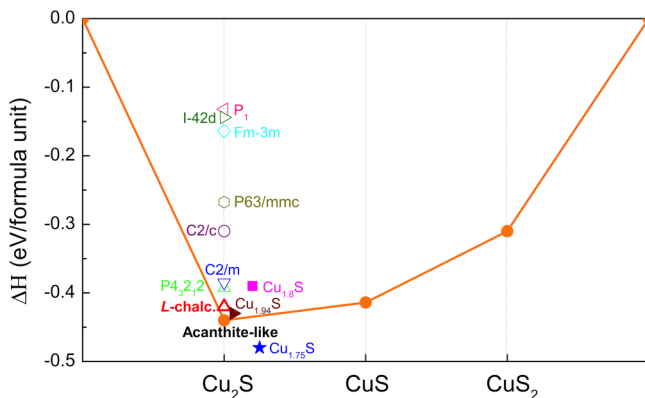


FIG. 1. Formation enthalpy per formula unit of three stoichiometric compounds of Cu-S system. Several structures of Cu_2S (unfilled color symbols) and different compounds (filled color symbols) taken from material project database [46] are also calculated for comparison.

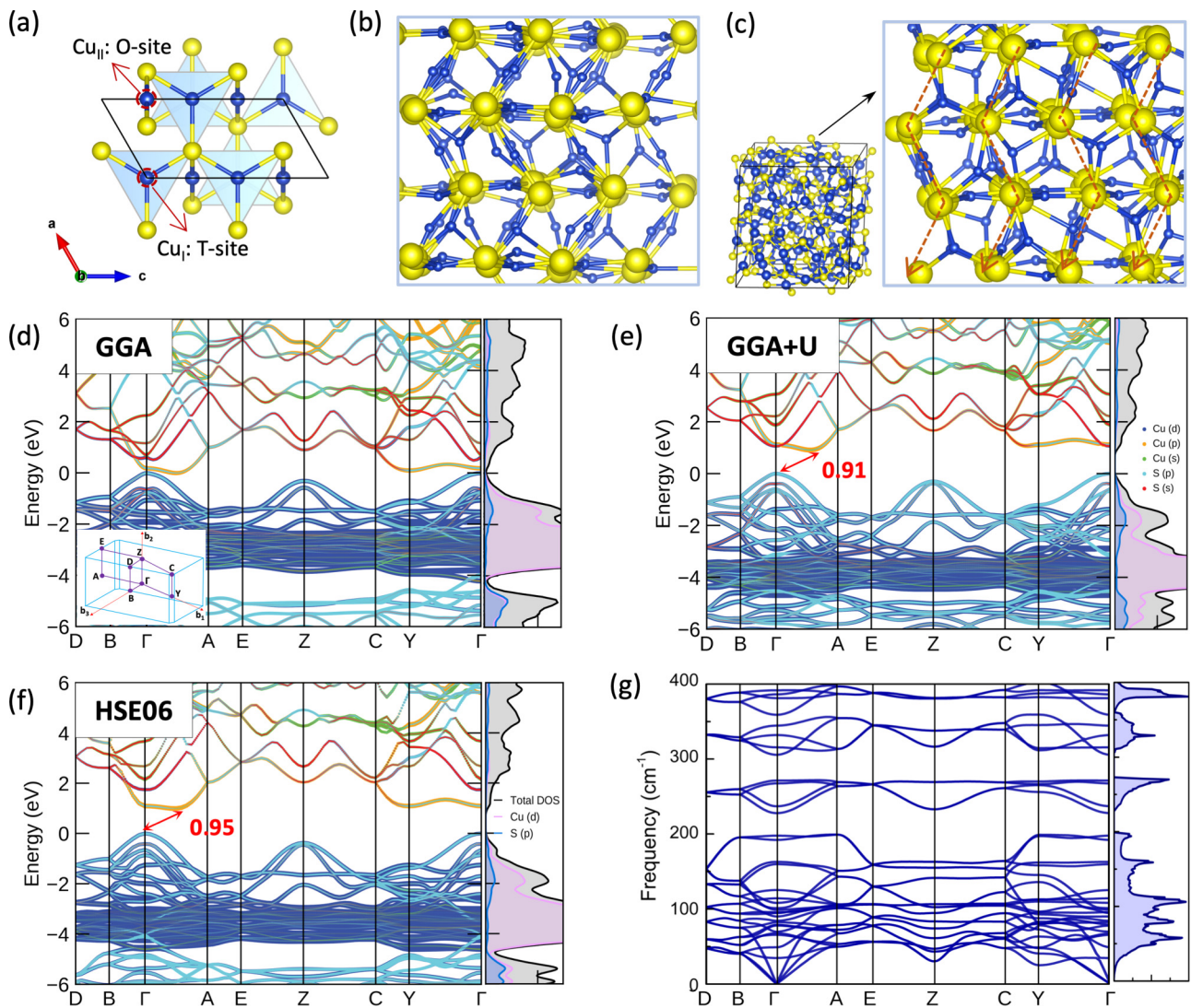


FIG. 2. (a) Crystal structure of Cu_2S acanthite-like phase (Cu atom: blue, S atom: yellow) where Cu occupied two significant positions, tetrahedral-site (Cu_I) and octahedral-site (Cu_{II}). (b) The displacement of Cu atoms in the acanthite-like phase via *ab initio* molecular dynamics simulation at 300 K shows similar behavior to the one in the low-chalcocite phase observed in experiments (c), where the S sublattice is nearly immobile with the zig-zag arrangement. (d)–(f) Electronic band structure, Brillouin zone, and DOS of Cu_2S acanthite-like phase by different functionals (Fermi energy is referred to the top of valence band); (g) Phonon dispersion and phonon DOS of acanthite-like phase.

hybridization between the *s* and *p* orbitals of Cu, *s* orbitals of S forms the CB. The band-gap estimation of both functionals is still lower than the experimental one, but these values are still reasonable for us to continue investigating other properties of the system.

Cu_2S is known to be a good solar absorber, so it is often fabricated in thin-film form or used as a dopant to increase absorption efficiency [47]. The high optical absorption coefficient of a material (usually characterized by $\alpha > 10^4 \text{ cm}^{-1}$) is important to achieve a good photovoltaic performance. The bandgap of Cu_2S is in the optimal 1.1–1.7 eV range required for high conversion efficiency as predicted in the Shockley-Queisser limit [48]. Although the bandgap was underestimated by about 17% for GGA + *U* and 13% for HSE06 functional, both functionals showed a similar trend with a significant increase in α values just about 0.3 eV above the bandgap, as depicted in Fig. 3(a). The absorption coefficients

become characteristic at about 1.8 eV, which is just at the start point of the visible spectrum and increases sharply thereafter. The results calculated by GGA + *U* functional are greater than those described for HSE06 functional in general, but these values obtained are larger than 10^4 , which is completely competitive with an indirect band-gap absorber as Si [49]. In addition, the transition probabilities between the two states of the VBM and CBM as shown in Fig. 3(b) are also revealed in the forbidden or allowed transition state. Accordingly, both functionals agree that the TDM amplitude between VBM and CBM at the Γ point is zero, indicating that there is no optical absorption between these two states. In contrast, strong optical absorption is observed along the direction of Γ –A or C–Y. These sites are the lowest points of CB, with the distance to VB falling at around 2.0 eV. This explains why the magnitude of the absorption coefficient increases sharply from this energy level of the visible spectrum.

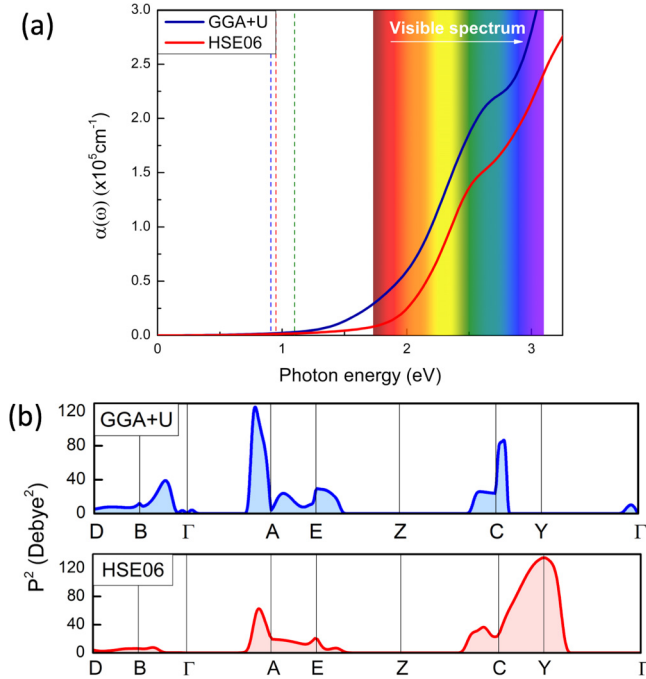


FIG. 3. (a) Absorption coefficient as a function of photon energy by GGA + U and HSE06 functionals in the range of the visible light spectrum. The bandgap energy marked by vertical dashed lines (navy: GGA + U , red: HSE06, green: experiment data). (b) Transition probability of electric dipole moment between two states of VB-CB along high-symmetry k points.

B. Intrinsic point defects formation

It has been reported that at the stoichiometric limit, Cu_2S is more stable in the L -chalc. structure [45]. However, this research also revealed that Cu_2S is not stable against the formation of Cu vacancies and Cu_7S_4 ($\text{Cu}_{1.75}\text{S}$) is the most stable structure of Cu_xS ($1.2 < x \leq 2.0$) system. Therefore, only competing stoichiometric phases are used for the determination of growth conditions of the acanthite-like phase. As shown in Fig. 4, the two intersection points bounding the stability region of Cu_2S acanthite-like phase in the plane ($\Delta\mu_{\text{Cu}}$, $\Delta\mu_{\text{S}}$). As a typical growth condition, we assume a Cu-rich condition ($\Delta\mu_{\text{Cu}} = 0 \text{ eV}$, $\Delta\mu_{\text{S}} = -0.44 \text{ eV}$) and a Cu-poor condition ($\Delta\mu_{\text{Cu}} = -0.03 \text{ eV}$, $\Delta\mu_{\text{S}} = -0.38 \text{ eV}$). Then, intrinsic defect formation energies of vacancies, interstitial atoms, and antisite atoms are calculated. Previous studies involving chalcopyrite families such as AgSbTe_2 , CuInSe_2 , CuGaO_2 , CuFeS_2 showed that they are semiconductors with predominant p -type defects [50–52]. A common feature that can be observed for this group is the appearance of antibonding states between cations and anions below the Fermi level. Consequently, these systems are often structurally unstable and likely to transfer to a more stable form, so that the bonding between cation-anion tends to be easily broken, potentially revealing the formation of defects such as vacancy in the system. Figure 5(a) gives us a view of the crystal orbital Hamiltonian population (COHP) curves between Cu and S in both sites of Cu. Clearly, there is an anti-bonding state between Cu-S at both sites, which is similar to that of the chalcopyrite family. Hence, it leads us to a prediction that p -type defects can be the

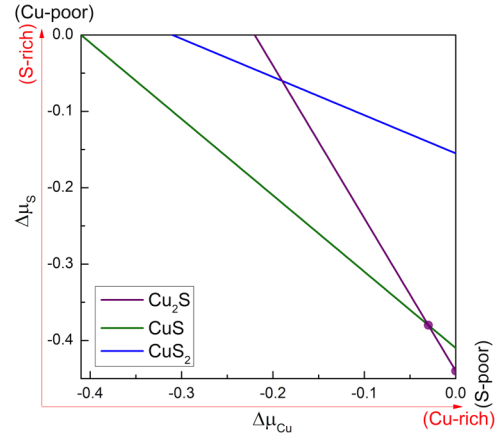


FIG. 4. Calculated chemical potentials of $\Delta\mu_{\text{Cu}}$ and $\Delta\mu_{\text{S}}$ for three stoichiometric compounds as competing phases, where the allowed region for the growth of Cu_2S is limited up to two intersection points.

predominant type of defects in the system. To strengthen the above assessment, we further consider the propensity of defects formation based on the energy aspect [see Fig. 5(b)].

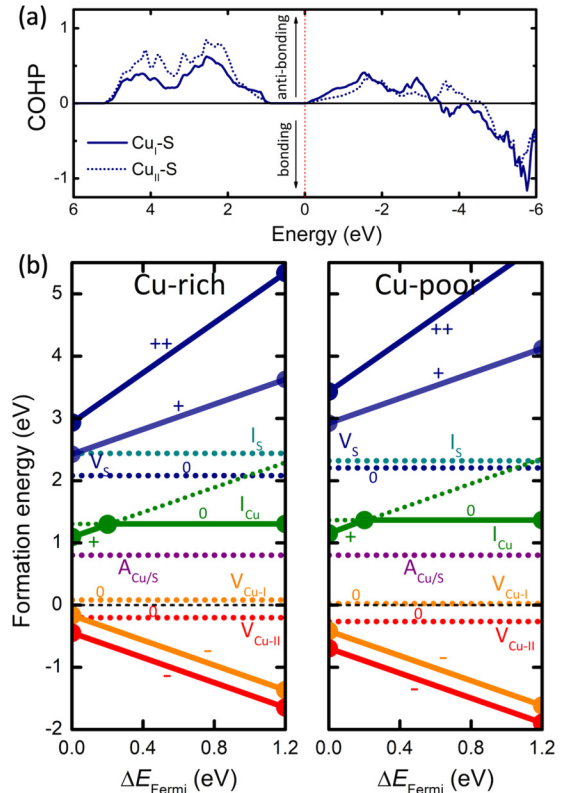


FIG. 5. (a) COHP curves of Cu-S bonding where Fermi level (black dashed line) is located at VBM (negative value: bonding nature, positive value: antibonding nature), (b) Formation energy of Cu_2S with different kinds of defects as a function of Fermi level under Cu-rich and Cu-poor conditions. The width of bandgap energy corresponds to horizontal axis values where the VBM point referred to the zero value.

Depending on growth conditions, the formation energies of Cu vacancy at two order positions differ by about 0.16–0.22 eV. Specifically, in the Cu-rich condition, a formation energy of neutral Cu vacancy at the O site (i.e., $V_{\text{Cu-II}} = -0.227$ eV) is smaller than that of the T site (i.e., $V_{\text{Cu-I}} = 0.06$ eV). It means the O site is more likely to generate Cu vacancies compared to T site. In Cu-poor condition, this energy decreases ($V_{\text{Cu-II}} = -0.257$ eV, $V_{\text{Cu-I}} = 0.03$ eV), resulting in more Cu vacancies forming. Moreover, formation energies are nearly zero or negative values at the Cu positions, indicating Cu vacancy is a typical intrinsic defect that is extremely easy to form in this system. As a result, the loss of electrons causes the shift of Fermi level to the VB, which is identified as an acceptor or p -type defect. This result is consistent with the COHP calculation shown in Fig. 5(a). Our calculations also show that Cu vacancies have lower formation energies when accepting one electron and transferring to the charged state -1 . Because the charged state transition between $0/-1$ occurs outside the band-gap energy range, the charged state of the Cu vacancy is preferred over the neutral state. In comparison to Cu vacancy, the formation energy of the S vacancy indicates that it is virtually hard to form, with an energy of around 2.15–2.20 eV. Because the neutral state is supposed to be more stable, the charged state transitions between $0/+1$ and $+1/+2$ are essentially nonexistent in the case of S vacancy. In contrast, the interstitial Cu atoms act as n -type defects in the compound. This type of defect might arise in both Cu-rich and Cu-poor conditions due to a minor difference in energy (only 0.03 eV). As can be seen, there is a charged state transition between $+1/0$ that occurs at 0.21 eV above the VBM. The charged state $+1$ of interstitial Cu shows that it is more stable than the neutral state for $\Delta E_{\text{Fermi}} < 0.21$ eV. Above the transition point ($\Delta E_{\text{Fermi}} > 0.21$ eV), the system switches from one electron-loss to a neutral charge. Similar results are also observed in the case of Ag_2S [53], where the presence of the positively charged interstitial atoms and negatively charged vacancies contribute to the charge neutralization of the system. However, because the interstitial atoms are not as energetically favored as they are in the case of Ag_2S , the predominance of Cu vacancies can be the reason for conductive behavior as a p -type semiconductor of Cu_2S , which is shown in the latter part. In the case of interstitial S atoms, the high formation energy (about 2.31–2.37 eV) suggests that it is unlikely to form and dominate in the system over other defects. Compared to the interstitial S atoms, the antisite defects are supposed to be more easily formed in the compound with an energy of around 0.8 eV. However, the presence of this kind of defect essentially does not change the transport properties of Cu_2S .

As the most predominant and easily formed defect in the system, it is important to know the diffusion mechanism of Cu vacancy. Here, the MEP is the favored migration path of atoms. Vacancy migration along the possible pathways that we consider here include three main ways: from T site to T site or $V_{\text{T}}-V_{\text{T}}$ (p_1), O site to O site or $V_{\text{O}}-V_{\text{O}}$ (p_2), and O site to T site to O site or $V_{\text{O}}-V_{\text{T}}-V_{\text{O}}$ (p_3), as shown in Fig. 6(a). The MEP of Cu vacancy as depicted in Fig. 6(b) shows that the maximum energy barrier of p_1 reaches a value of about 1 eV, which is high enough to challenge the atoms to overcome. Therefore, the migration of the vacancies, of course, hardly

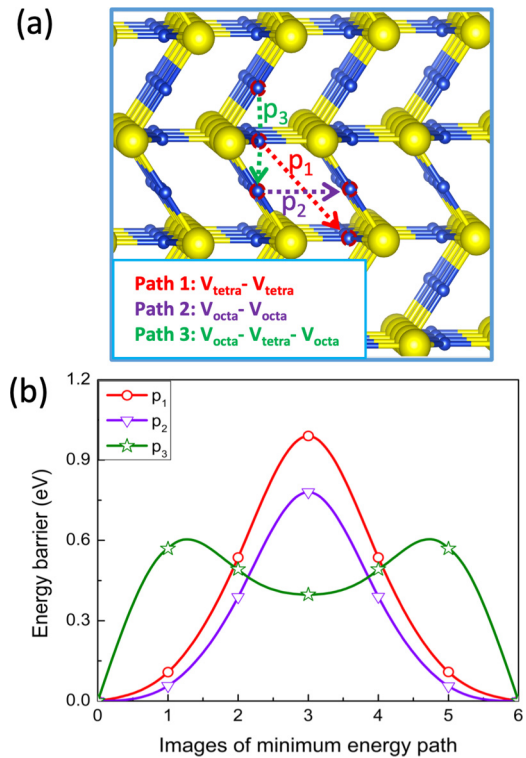


FIG. 6. (a) Three possible diffusion pathways of Cu vacancy. (b) MEP of Cu vacancy from T site to T site (p_1), O site to O site (p_2), and O site to T site to O site (p_3).

takes place in this route. Compared with the p_1 route, Cu vacancies are considered to diffuse more easily through the p_2 route because the highest energy barrier is only about 0.78 eV. However, the p_3 route could be the preferred migration path for Cu vacancies based on energy aspects. In this way, they just need to overcome a maximum energy barrier of around 0.58 eV from the first O site to approach the local minimum of the adjacent T site located at 0.4 eV, and then diffuse to the next neighboring O site, which is easier than the rest of the pathways. A similar migration trend can be found in the case of Ag_2S [54].

C. Transport properties: Electron-phonon coupling

There are several approaches to determining the transport properties using the Boltzmann theory. The use of the constant relaxation-time approximation (CRTA) is perhaps the most common and also accessible approach. However, this strategy often works in systems with good electrical conductors, where the electron energy relaxation time varies very slightly with electron energy, allowing us to regard it as a constant [42]. Ascertaining electrical conductivity is more challenging because relaxation time is a direct factor that largely affects the accuracy. As a result, using CRTA for determining this parameter can be a poor approach. Therefore, we should adopt the EPA approach as the main scattering mechanism for our system. In addition, due to the mobility nature of Cu atoms in the compound, strongly scattered phonons can occur to reduce the phonon mean free path and also omit sectional lattice vibration modes to lessen the specific heat. Thus, lattice

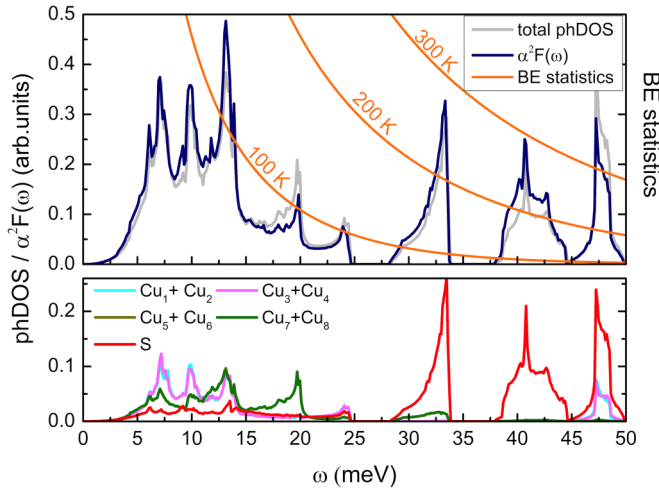


FIG. 7. The Eliashberg spectral function $\alpha^2 F(\omega)$ and the total phonon density of states (phDOS) of Cu_2S (figure above) and the partial phDOS (figure below). The solid orange lines show Bose-Einstein statistics for three lattice temperatures.

thermal conductivity can be optimally reduced, resulting in an extremely low κ value of Cu_2S [9,55]. Hereinafter, we only focus on the electronic part of conductivity.

The Eliashberg spectral function $\alpha^2 F(\omega)$ is a combination of phonon DOS $F(\omega)$ and the phonon frequency-dependent electron-phonon coupling $\alpha^2(\omega)$. In this way, all allowed scattering processes of electrons with phonons of frequency ω can be observed, as shown in Fig. 7. Specifically, phonons obey Bose-Einstein statistics in a thermal state at different temperatures. Strong couplings of electrons to phonons can be observed in the ranges of 10–15, 30–35, and 40–45 meV when compared with phonon DOS. In particular, from 10 to 15 meV, the magnitude of the Eliashberg function is enhanced due to the strong coupling that occurs on the Cu side (dominated by Cu_1 , Cu_2 , Cu_3 , and Cu_4). While, the strongest coupling occurs in the high-frequency range of 30–45 meV, it is mainly caused by scattering on the S side, where phonon occupation is getting lower in the thermal state. This can be a consequence of the energy transferring between electrons and lattice in non equilibrium states, resulting in transient nonthermal phonon distributions [56]. Thereafter, the energy dependence of electron relaxation time is calculated and depicted in Fig. 8. As can be seen, the τ value shows strong energy dependence and increases sharply near the band edges. This behavior can be explained by the relation

$$\tau^{-1}(\epsilon) \sim g^2(\epsilon)\rho(\epsilon), \quad (17)$$

where τ is inversely proportional to ρ while electron-phonon matrix element g^2 shows a weak carrier energy dependency. Because of the strong energy dependence, the contribution of τ can be considered paramount, especially for conductivity determination. To facilitate comparison, the results from the CRTA method are also taken into account (here, a $\tau = \tau_{\text{const}} = 10$ fs [53] is used). Transport parameters are shown in Fig. 9. Although experimental evidence suggests that the major carrier of Cu_2S is p type, which agrees with our predictions of the favored-intrinsic defect kind stated previously, we will

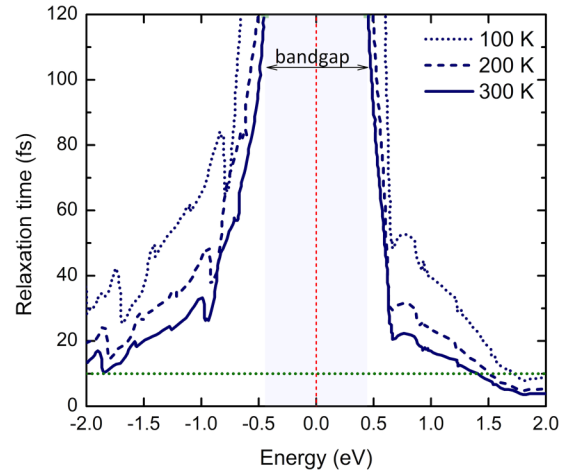


FIG. 8. The electron energy relaxation time τ as a function of the electron energy ϵ at different temperature ranges. The light navy color bar denotes the bandgap area. Fermi level (red dashed line) is located in the middle of bandgap. Here, $\tau = 10$ fs (green dashed line) also is used for CRTA method.

analyze both p - and n -type conductive behaviors from a theoretical standpoint below.

Looking at the p -type case first, it is clear that the EPA method estimates the Seebeck coefficients slightly lower than the CRTA method at all carrier concentrations. For instance, at $n = 10^{17} \text{ cm}^{-3}$ and $T = 320$ K, the CRTA and EPA yield the Seebeck coefficient of 661 and $607 \mu\text{V K}^{-1}$. Meanwhile, these values reach 476 and $410 \mu\text{V K}^{-1}$ at $n = 10^{18} \text{ cm}^{-3}$, respectively. Overall, there are no major differences in trend and magnitude for both methods. This is understandable because of the weak dependence of the Seebeck coefficient on τ , which can be eliminated approximately in some cases due to the involvement of τ in both numerator and denominator, as shown in Eq. (10). It should be noted that the Seebeck coefficients reported in previous experimental works show a scattering of several hundred $\mu\text{V K}^{-1}$ (e.g., at 325 K, the different studies also give different values of around $600 \mu\text{V K}^{-1}$ [57], $310 \mu\text{V K}^{-1}$ [58], and $140 \mu\text{V K}^{-1}$ [55]), possibly as a result of differences in sample fabrication methods. This leads to the variation in carrier concentration of these samples, staying around 10^{17} – 10^{18} cm^{-3} . In this case, the EPA gives an estimate that is closer to the experimental value than the CRTA. The difference between the two methods only becomes significant when estimating conductivity.

The τ value is considered a constant in the CRTA approach, and thus only changes in carrier concentration might not greatly affect conductivity. As can be seen, σ values hardly improved as the temperature and doping concentration increased. In particular, the change in carrier concentrations at 300 K of 10^{15} , 10^{16} , 10^{17} , and 10^{18} cm^{-3} leads to a corresponding change in conductivity of 0.54, 5.1, 50.6, and 506 Sm^{-1} . That is an improvement of about 10 times in terms of magnitude. Only when increasing the concentration to 10^{18} – 10^{19} cm^{-3} , σ values in experimental measurements are reproduced. Meanwhile, the electron-phonon scattering model shows that τ is strongly dependent on energy. This dependence thus reflects the significant enhancement of

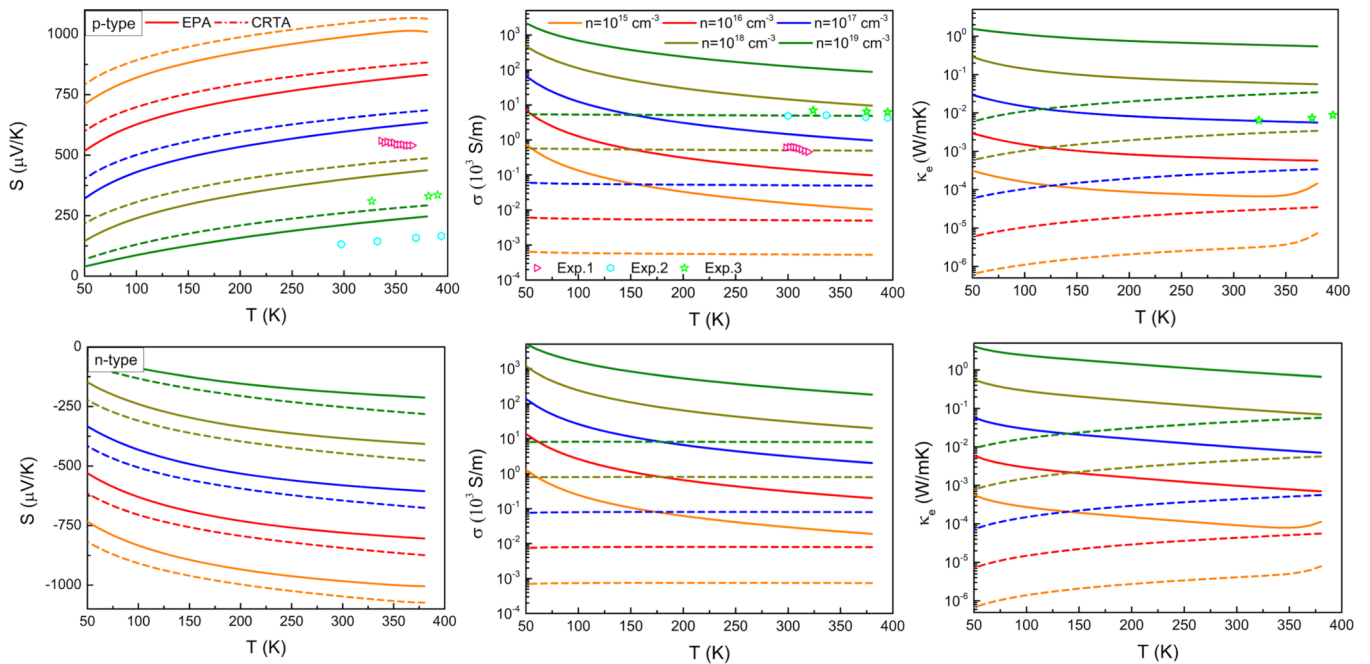


FIG. 9. Transport parameters of Cu_2S acanthite-like phase including Seebeck coefficient (S), electrical conductivity (σ), and electronic thermal conductivity (κ_e) as a function of temperature at different carrier concentrations. The straight lines indicate theoretical estimation by the EPA method while the dashed lines illustrate results from the CRTA method. Here, data from previous experiment works [55,57,58] is also included for comparison.

σ with each increase in doping concentration. The σ values were determined using the EPA approach at the same doping concentrations as the CRTA method, but the results were 15.6, 147.7, 1465.8, and 14449.1 Sm^{-1} , respectively. The difference in the estimated σ values between the EPA and CRTA approaches under the same conditions is rather considerable in this case. In other words, the EPA method can give a reasonable estimation at the same concentration as the actual measurement [57,58], while the CRTA method requires increasing the doping concentration by a minimum of ten times for a similar prediction.

Similar results are also observed in the case of κ_e . At $n = 10^{18} \text{ cm}^{-3}$ and 300 K, CRTA method for predictive κ_e value is $0.0028 \text{ Wm}^{-1} \text{ K}^{-1}$. The significant difference in magnitude by the CRTA method only occurred when the doping concentration was up to 10^{19} cm^{-3} (i.e., $0.0283 \text{ Wm}^{-1} \text{ K}^{-1}$). Meanwhile, κ_e values of the same concentration as described by EPA method were 200 times as large (e.g, $0.065 \text{ Wm}^{-1} \text{ K}^{-1}$ at 10^{18} cm^{-3} and $0.62 \text{ Wm}^{-1} \text{ K}^{-1}$ at 10^{19} cm^{-3}). Of course, we can control the τ value in the CRTA method to best fit the experiment data, but the EPA method plainly shows an advantage in reasonably predicting τ . Thus, rather than employing τ as an input constant, it is critical to account for it in conductivity prediction.

When considering n -type doping, a similar tendency can be seen. The difference between n -type and p -type doping in terms of Seebeck value is not significant. Although it is difficult to produce an n -type conductive sample for Cu_2S in reality, enhancing point defects as interstitial Cu atoms can help strengthen the n -type carriers. As a result, the conductivity can theoretically be larger than that of p -type doping. However, it should be mentioned that in the low-temperature

range, the EPA method tends to overestimate electrical and thermal conductivity values. This is understandable since other scattering mechanisms including impurities, defects, and alloy disorders are ignored in this approximation. Therefore, the addition of these processes in future work could improve the prediction in the low-temperature range.

Finally, the relation between energy-dependent relaxation time and doping concentration is shown in Fig. 10. We define the effective value of electronic relaxation time as $\bar{\tau} = \tau_{\text{crtA}} \sigma_{\text{epa}} / \sigma_{\text{crtA}}$, which roughly corresponds to the average of τ_{epa} at different doping concentrations. Note that $\bar{\tau}$ does not

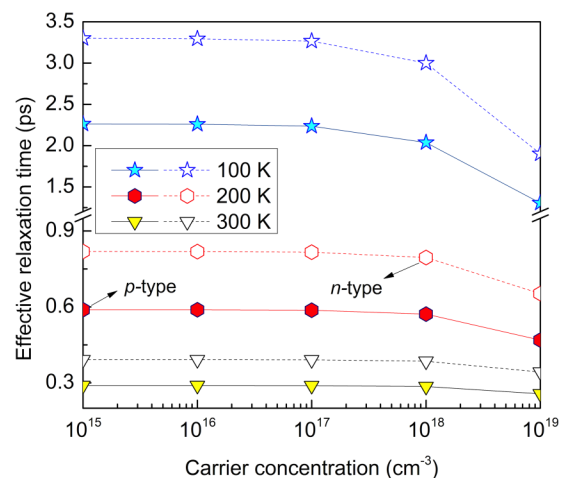


FIG. 10. The electron energy relaxation time $\bar{\tau}$ as a function of doping concentrations at different temperature ranges for both p -type (filled color symbols) and n -type cases (unfilled-color symbols).

depend on τ_{crt} because $\sigma_{\text{crt}} \propto \tau_{\text{crt}}$ by definition. Changing the doping concentration in the system controls the shift of the chemical potential toward the VB (*p* type) or CB (*n* type). At the same temperature and doping concentration, the relaxation time values reveal that there is stronger scattering occurring near the VB, resulting in a lower value of relaxation time here than near the CB. Furthermore, an increase in the doping concentration resulted in a decrease in the relaxation time values at all concentrations, with minor changes at low concentrations (10^{15} – 10^{17} cm⁻³) and larger decreases at higher concentrations (10^{18} – 10^{19} cm⁻³). This can be the result of increased scattering events of high-energy phonons in the system in the presence of high doping concentrations.

IV. CONCLUSIONS

In summary, we have performed first-principles calculations incorporating the Boltzmann theory in computing the electronic properties, intrinsic defect formation, and electron-phonon scattering model to estimate the transport properties of Cu₂S using an acanthite-like model. This theoretical

structure not only simplifies the calculation but also confirms the indirect nature of the band gap as observed before in the experiment. Intrinsic defect formation shows Cu vacancy formation as the most favored defect based on both bonding analysis and energy aspects. Finally, the comparison between the CRTA and the EPA method helps to highlight the suitability of the electron-phonon scattering mechanism in predicting the transport properties of Cu₂S. For the main purpose, we demonstrate that the acanthite-like model is ideally suitable and can be used for TE material design purposes related to the low-temperature phase of Cu₂S.

ACKNOWLEDGMENTS

This research was supported by JST CREST (Grant No. JP-MJCR18I2). H.N.N. acknowledges the financial support from the Ministry of Education, Culture, Sports, Science, and Technology (MEXT) and Research Grant for Innovative Asia program of Japan International Cooperation Agency (JICA). H.N.N. also thanks H.B. Tran and H. Okumura for their valuable help.

-
- [1] L. E. Bell, *Science* **321**, 1457 (2008).
 - [2] F. J. Disalvo, *Science* **285**, 703 (1999).
 - [3] C. Li, F. Jiang, C. Liu, P. Liu, and J. Xu, *Appl. Mater. Today* **15**, 543 (2019).
 - [4] X.-L. Shi, J. Zou, and Z.-G. Chen, *Chem. Rev.* **120**, 7399 (2020).
 - [5] S. Ghodke, O. Muthusamy, K. D. Codrin, S. Choi, S. Singh, D. Byeon, M. Adachi, M. Kiyama, T. Matsuura, Y. Yamamoto, M. Matsunami, and T. Takeuchi, [arXiv:1909.12476](https://arxiv.org/abs/1909.12476).
 - [6] M. Beekman, D. T. Morelli, and G. S. Nolas, *Nat. Mater.* **14**, 1182 (2015).
 - [7] G. A. Slack, *CRC Handbook of Thermoelectrics* (CRC Press, Boca Raton, FL, 1995).
 - [8] H. Liu, X. Shi, F. Xu, L. Zhang, W. Zhang, L. Chen, Q. Li, C. Uher, T. Day, and G. J. Snyder, *Nat. Mater.* **11**, 422 (2012).
 - [9] Z. Zhang, K. Zhao, T.-R. Wei, P. Qiu, L. Chen, and X. Shi, *Energy Environ. Sci.* **13**, 3307 (2020).
 - [10] X. Shi, H. Chen, F. Hao, R. Liu, T. Wang, P. Qiu, U. Burkhardt, Y. Grin, and L. Chen, *Nat. Mater.* **17**, 421 (2018).
 - [11] D. Byeon, R. Sobota, K. Delime-Codrin, S. Choi, K. Hirata, M. Adachi, M. Kiyama, T. Matsuura, Y. Yamamoto, M. Matsunami, and T. Takeuchi, *Nat. Commun.* **10**, 72 (2019).
 - [12] S. Singh, K. Hirata, D. Byeon, T. Matsunaga, O. Muthusamy, S. Ghodke, M. Adachi, Y. Yamamoto, M. Matsunami, and T. Takeuchi, *J. Electron. Mater.* **49**, 2846 (2020).
 - [13] S. Deng, X. Jiang, L. Chen, N. Qi, X. Tang, and Z. Chen, *ACS Appl. Mater. Interfaces* **13**, 868 (2021).
 - [14] J. A. Bragagnolo, A. M. Barnett, J. E. Phillips, R. B. Hall, A. Rothwarf, and J. D. Meakin, *IEEE Trans. Electron Devices* **27**, 645 (1980).
 - [15] L. Isac, I. Popovici, A. Enesca, and A. Duta, *Energy Procedia* **2**, 71 (2010).
 - [16] D. S. Nkemini, Z. Yang, S. Lou, G. Li, and S. Zhou, *J. Alloys Compd.* **878**, 160128 (2021).
 - [17] U. Ryuzo, *J. Phys. Soc. Jpn.* **4**, 287 (1949).
 - [18] M. J. Buerger and B. J. Wuensch, *Science* **141**, 276 (1963).
 - [19] H. T. J. Evans, Jr., *Z. Kristallogr.* **150**, 299 (1979).
 - [20] R. W. Potter, *Econ. Geol.* **72**, 1524 (1977).
 - [21] P. Lukashev, W. R. L. Lambrecht, T. Kotani, and M. van Schilfgaarde, *Phys. Rev. B* **76**, 195202 (2007).
 - [22] L.-W. Wang, *Phys. Rev. Lett.* **108**, 085703 (2012).
 - [23] P. S. McLeod, L. D. Partain, D. E. Sawyer, and T. M. Peterson, *Appl. Phys. Lett.* **45**, 472 (1984).
 - [24] L. D. Partain, P. S. McLeod, J. A. Duisman, T. M. Peterson, D. E. Sawyer, and C. S. Dean, *J. Appl. Phys.* **54**, 6708 (1983).
 - [25] B. Sadtler, D. O. Demchenko, H. Zheng, S. M. Hughes, M. G. Merkle, U. Dahmen, L.-W. Wang, and A. P. Alivisatos, *J. Am. Chem. Soc.* **131**, 5285 (2009).
 - [26] P. Khatri, A Structural Prediction of Copper Sulfide and Study of Its Electronic Properties and Vacancy Forming Trend Using Density Functional Theory, M.S. thesis, Department of Physics, The University of Texas at Arlington, 2014. <http://hdl.handle.net/10106/25569>
 - [27] P. Khatri and M. N. Huda, *Int. J. Photoenergy* **2015**, 478978 (2015).
 - [28] S. K. Barman and M. N. Huda, *J. Phys.: Condens. Matter* **30**, 165701 (2018).
 - [29] S. K. Barman and M. N. Huda, *J. Appl. Phys.* **128**, 015703 (2020).
 - [30] G. Kresse and J. Furthmüller, *Phys. Rev. B* **54**, 11169 (1996).
 - [31] G. Kresse and D. Joubert, *Phys. Rev. B* **59**, 1758 (1999).
 - [32] J. P. Perdew, K. Burke, and M. Ernzerhof, *Phys. Rev. Lett.* **77**, 3865 (1996).
 - [33] J. A. Suárez, J. J. Plata, A. M. Márquez, and J. F. Sanz, *Theor. Chem. Acc.* **135**, 70 (2016).
 - [34] A. V. Krugau, O. A. Vydrov, A. F. Izmaylov, and G. E. Scuseria, *J. Chem. Phys.* **125**, 224106 (2006).
 - [35] H. Jónsson, G. Mills, and K. W. Jacobsen, *Classical and Quantum Dynamics in Condensed Phase Simulations* (World Scientific, Singapore, 1998), pp. 385–404.

- [36] M. Fox, *Optical Properties of Solids* (Oxford University Press, New York, 2002).
- [37] V. Wang, N. Xu, J.-C. Liu, G. Tang, and W.-T. Geng, *Comput. Phys. Commun.* **267**, 108033 (2021).
- [38] S. G. Louie and A. Rubio, *Handbook of Materials Modeling: Methods*, edited by S. Yip (Springer Netherlands, Dordrecht, 2005), pp. 215240.
- [39] C. G. de Walle and J. Neugebauer, *J. Appl. Phys.* **95**, 3851 (2004).
- [40] P. Giannozzi, S. Baroni, N. Bonini, M. Calandra, R. Car, C. Cavazzoni, D. Ceresoli, G. L. Chiarotti, M. Cococcioni, I. Dabo, A. D. Corso, S. de Gironcoli, S. Fabris, G. Fratesi, R. Gebauer, U. Gerstmann, C. Gougoussis, A. Kokalj, M. Lazzeri, L. Martin-Samos *et al.*, *J. Phys.: Condens. Matter* **21**, 395502 (2009).
- [41] G. K. H. Madsen and D. J. Singh, *Comput. Phys. Commun.* **175**, 67 (2006).
- [42] G. Samsonidze and B. Kozinsky, *Adv. Energy Mater.* **8**, 1800246 (2018).
- [43] M. Wierzbowska, S. de Gironcoli, and P. Giannozzi, [arXiv:cond-mat/0504077](https://arxiv.org/abs/cond-mat/0504077).
- [44] S. Ponc e, E. R. Margine, C. Verdi, and F. Giustino, *Comput. Phys. Commun.* **209**, 116 (2016).
- [45] Q. Xu, B. Huang, Y. Zhao, Y. Yan, R. Noufi, and S. H. Wei, *Appl. Phys. Lett.* **100**, 061906 (2012).
- [46] A. Jain, S. P. Ong, G. Hautier, W. Chen, W. D. Richards, S. Dacek, S. Cholia, D. Gunter, D. Skinner, G. Ceder, and K. Persson, *APL Mater.* **1**, 011002 (2013).
- [47] Y. Lv, J. Chen, R.-K. Zheng, J. Song, T. Zhang, X. Li, X. Shi, and L. Chen, *Sci. Rep.* **5**, 16291 (2015).
- [48] S. R uhle, *Sol. Energy* **130**, 139 (2016).
- [49] K. Rajkanan, R. Singh, and J. Shewchun, *Solid. State. Electron.* **22**, 793 (1979).
- [50] H. Shinya, A. Masago, T. Fukushima, and H. Katayama-Yoshida, *Jpn. J. Appl. Phys.* **55**, 41801 (2016).
- [51] A. Zakutayev, C. M. Caskey, A. N. Fioretti, D. S. Ginley, J. Vidal, V. Stevanovic, E. Tea, and S. Lany, *J. Phys. Chem. Lett.* **5**, 1117 (2014).
- [52] S. B. Zhang, S.-H. Wei, A. Zunger, and H. Katayama-Yoshida, *Phys. Rev. B* **57**, 9642 (1998).
- [53] H. Ngoc Nam, R. Yamada, H. Okumura, T. Q. Nguyen, K. Suzuki, H. Shinya, A. Masago, T. Fukushima, and K. Sato, *Phys. Chem. Chem. Phys.* **23**, 9773 (2021).
- [54] Z. Wang, T. Gu, T. Kadohira, T. Tada, and S. Watanabe, *J. Chem. Phys.* **128**, 14704 (2008).
- [55] Y. Yao, B.-P. Zhang, J. Pei, Y.-C. Liu, and J.-F. Li, *J. Mater. Chem. C* **5**, 7845 (2017).
- [56] L. Waldecker, R. Bertoni, R. Ernstorfer, and J. Vorberger, *Phys. Rev. X* **6**, 021003 (2016).
- [57] D. Byeon, R. Sobota, K. Hirata, S. Singh, S. Choi, M. Adachi, Y. Yamamoto, M. Matsunami, and T. Takeuchi, *J. Alloys Compd.* **826**, 154155 (2020).
- [58] H. Gong, X.-L. Su, Y.-G. Yan, and X.-F. Tang, *J. Inorg. Mater.* **34**, 1295 (2019).